

Magnetic nanoparticle imaging by means of minimum norm estimates from remanence measurements

Daniel Baumgarten · Mario Liehr · Frank Wiekhorst ·
Uwe Steinhoff · Peter Münster · Peter Miethe ·
Lutz Trahms · Jens Haueisen

Received: 28 January 2008 / Accepted: 19 September 2008 / Published online: 8 October 2008
© International Federation for Medical and Biological Engineering 2008

Abstract In magnetic nanoparticle imaging, magnetic nanoparticles are coated and functionalized to bind to specific targets. After measuring their magnetic relaxation or remanence, their distribution can be determined by means of inverse methods. The reconstruction algorithm presented in this paper includes first a dipole fit using a Levenberg–Marquardt optimizer to determine the reconstruction plane. Secondly, a minimum norm estimate is obtained on a regular grid placed in that plane. Computer simulations involving different parameter sets and conditions show that the used approach allows for the reconstruction of distributed sources, although the reconstructed shapes are distorted by blurring effects. The reconstruction quality depends on the signal-to-noise ratio of the measurements and decreases with larger sensor-source distances and higher grid spacings. In phantom

measurements, the magnetic remanence of nanoparticle columns with clinical relevant sizes is determined with two common measurement systems. The reconstructions from these measurements indicate that the approach is applicable for clinical measurements. Our results provide parameter sets for successful application of minimum norm approaches to Magnetic Nanoparticle Imaging.

Keywords Magnetic nanoparticle · Imaging · Minimum norm estimate · Magnetic remanence

1 Introduction

Magnetic particles with a diameter in the nanometer range—referred to as magnetic nanoparticles (MNP)—show a set of interesting properties including a high saturation magnetization and superparamagnetic behavior at room temperature. These properties give them a high potential for use in both medical diagnostics and therapy [15, 19, 22]. They are used for magnetic hyperthermia [14, 17], magnetic drug targeting [2, 6], cell separation [3], as labels in immunoassays [8, 30] and as contrast agents in MRI [5, 26]. The quantitative determination of the nanoparticle distribution over large tissue areas remains a challenge. To this end, a number of methods have been applied including contrast reduction in CT [16] and MRI [21] as well as magnetorelaxometry combined with tissue dissection [31]. Besides, magnetic particle imaging (MPI) shows potential to become a stand-alone in vivo particle imaging method [9, 10].

In this paper, we present a combination of magnetic nanoparticle immunoassays and magnetic imaging methods, termed as magnetic nanoparticle imaging (MNPI). For this technique, magnetic nanoparticles are coated and

D. Baumgarten (✉) · J. Haueisen
Institute of Biomedical Engineering and Informatics,
Technische Universität Ilmenau, P.O. Box 100565,
98684 Ilmenau, Germany
e-mail: daniel.baumgarten@tu-ilmenau.de

M. Liehr
Department of Internal Medicine I and Biomagnetic Center,
Department of Neurology, Friedrich Schiller University Jena,
07745 Jena, Germany

F. Wiekhorst · U. Steinhoff · L. Trahms
Physikalisch-Technische Bundesanstalt, 10587 Berlin, Germany

P. Münster
Senova GmbH, 07745 Jena, Germany

P. Miethe
fzmb GmbH, Research Centre of Medical Technology
and Biotechnology, Geranienweg 7,
99947 Bad Langensalza, Germany

functionalized to bind to specific targets in the human body. Their magnetic state is read out either by measurement of magnetic relaxation or magnetic remanence. In relaxation measurements, after switching off an externally applied magnetic field, the magnetization of an ensemble of particles relaxes by two different mechanisms. In particles that are bound to the target, only the magnetization vector reorientates (Néel relaxation) while unbound particles relax due to the motion of the particles themselves (Brown relaxation). From the measured relaxation behavior or magnetic remanence, respectively, the distribution of the bound particles and subsequently the location of the targets can be determined by means of inverse methods.

Like many other inverse problems, this determination is non-unique. An infinite number of particle distributions exist that can explain the measured field. A common method to reconstruct distributed sources without a priori knowledge are minimum norm estimates (MNE) [12, 29]. The sources are approximated by a number of dipoles in the region of interest, usually distributed over a regular grid. The parameters of these dipoles are then determined by linear estimation in the least-squares sense. Minimum norm methods have e. g. been used to reconstruct pipeline defects in nondestructive testing [13]. They have also been widely applied in the reconstruction of current sources from EEG and MEG measurements of the human brain and MCG measurements of the human heart [11, 18, 20].

The progress in the sensitivity of magnetic detection techniques now enables us to measure magnetic fields of magnetic particles with diameters of a few nanometers, today's computing capacities and sophisticated inverse methods allow for the reconstruction of distributed, magnetostatic sources using a high number of dipoles. The aim of our work is the *in vitro* and *in vivo* imaging of functionalized magnetic nanoparticles bound to specific targets. With this technique, the localization of cancer tumors and metastases or inflammations will be possible and their spatial extent can be determined. Furthermore, the distribution and absorption of administered drugs bound to nanoparticles can be observed. In contrast to known imaging methods, this technique allows for the quantification of the nanoparticle distributions. Besides, bound and unbound particles are dominated by different relaxation processes. Therefore, particles that are not bound to the targets do not contribute to the measured Néel relaxation or remanence signal and do not need to be washed out. In this paper we present a minimum norm approach for the reconstruction of the distribution of magnetic nanoparticles from magnetic remanence measurements. Our aim is the assessment of the performance of MNE in this application and, more specifically, the quantification of the influence of noise and the effects of the sensor-source distance and the reconstruction

grid on the inverse solution. For this purpose, we employ both computer simulations and remanence measurements on physical nanoparticle phantoms.

2 Methods

2.1 Forward and inverse problem

Essential for every inverse procedure is the knowledge of the forward solution that explains the field amplitude \mathbf{B} in the sensor points generated by the sources. This amplitude is either the relaxation amplitude in the case of relaxation measurements or directly the magnetic remanence signal. Since in our setup both values can be considered as time-independent, we use the static magnetic dipole model given in the following equation to compute the forward solution of the measurements:

$$\mathbf{B}(\mathbf{r}) = \frac{\mu_0}{4\pi} \left(\frac{3(\mathbf{m} \cdot \mathbf{r})\mathbf{r}}{r^5} - \frac{\mathbf{m}}{r^3} \right) \quad (1)$$

where \mathbf{B} is the magnetic field, \mathbf{r} is the vector from the position of the dipole to the position where the field is being measured, r is the absolute value of \mathbf{r} , i.e. the distance from the dipole, \mathbf{m} is the (vector) dipole moment and μ_0 is the permeability of free space. For static magnetic fields, provided no metallic implants exist, the relative permeability of biological tissue is approximately 1 and can therefore be ignored. Considering magnetic nanoparticles, a cluster of particles is modelled as a dipole. The magnetic field in the sensors is a linear superposition of the magnetic fields emanated by each modelled dipole. Applying minimum norm methods, the dipoles to be reconstructed are placed on fixed positions. The information on these source locations and the geometry of the sensor array is merged to the lead field matrix \mathbf{L} which links the dipole data vector \mathbf{m} with the forward computed data vector \mathbf{B}_f :

$$\mathbf{B}_f = \mathbf{L} \cdot \mathbf{m} \quad (2)$$

In our case this is an underdetermined system of equations as the number of sensors is generally smaller than the number of unknown dipole parameters. As we use MNEs for the inverse computation, the difference between the forward computed data \mathbf{B}_f and the measured field \mathbf{B}_m has to be minimized to find the optimal dipole parameters:

$$\Delta^2 = \|\mathbf{B}_f - \mathbf{B}_m\|^2 = \|\mathbf{L} \cdot \mathbf{m} - \mathbf{B}_m\|^2 \quad (3)$$

Introducing a Tikhonov regularization term [27] into Eq. 3 leads to

$$\Delta^2 = \|\mathbf{L} \cdot \mathbf{m} - \mathbf{B}_m\|^2 + \lambda \|\mathbf{W} \cdot \mathbf{m}\|^2 \quad (4)$$

with the regularization factor λ and the weighting matrix \mathbf{W} . The optimal parameters of the dipoles can then be estimated as

$$\hat{\mathbf{m}} = (\mathbf{L}^T \mathbf{L} + \lambda \mathbf{W}^T \mathbf{W})^{-1} \mathbf{L}^T \mathbf{B}_m \quad (5)$$

The reconstructions in this paper are all computed in two-dimensional planes. For determining the plane of interest, a single dipole model is fitted to the measured data using the Levenberg–Marquardt optimizer. The horizontal plane running through this dipole then serves as the reconstruction plane where the regular dipole grid is positioned. For this 2D computation we can use the identity matrix as the weighting matrix \mathbf{W} in Eq. 5.

All formulas and algorithms described above were implemented into the software toolbox SimBio [1] that provides a generic environment for electromagnetic source localization.

2.2 Computer simulation

To evaluate the performance of our approach to magnetic nanoparticle imaging we simulated different configurations of distributed sources involving realistic sensor positions from the setups described below. The fields of the simulated sources in these sensor positions were computed using Eq. 1. Figure 1 shows an example for a simulated source configuration with a realistic sensor-source distance of 40 mm (a), the amplitude of the magnetic field in the bottom sensor layer simulated with the PTB sensor configuration (b) and the sources reconstructed from the noiseless data using the minimum norm approach (c). For this computation the reconstruction plane was positioned in the plane of the simulated sources. Displayed are the dipoles in the grid nodes and their amplitudes. To investigate the reconstruction behavior under different conditions, sources with different sensor-source distances were simulated using various grid spacings. Additionally, the forward computed data were partially superimposed by white Gaussian noise before the inverse computations.

2.3 Nanoparticle phantoms

Besides the computer simulation we performed remanence measurements of physical magnetic nanoparticle phantoms using column phantoms from Senova GmbH Jena (see Fig. 2a). These columns contain polyethylene filters with an average pore size of 50 μm . For the phantom measurements the filters were coated with anti-*Streptococcus sobrinus* antibody. In a flow-through 3D-immunofiltration assay *S. sobrinus* (concentrations ranging from 10^3 to 10^5 CFU/ml) bound to the coated antibody. Magnetic nanoparticles fabricated by Chemagen GmbH, Baesweiler (average hydrodynamic diameter: 500–700 nm) containing

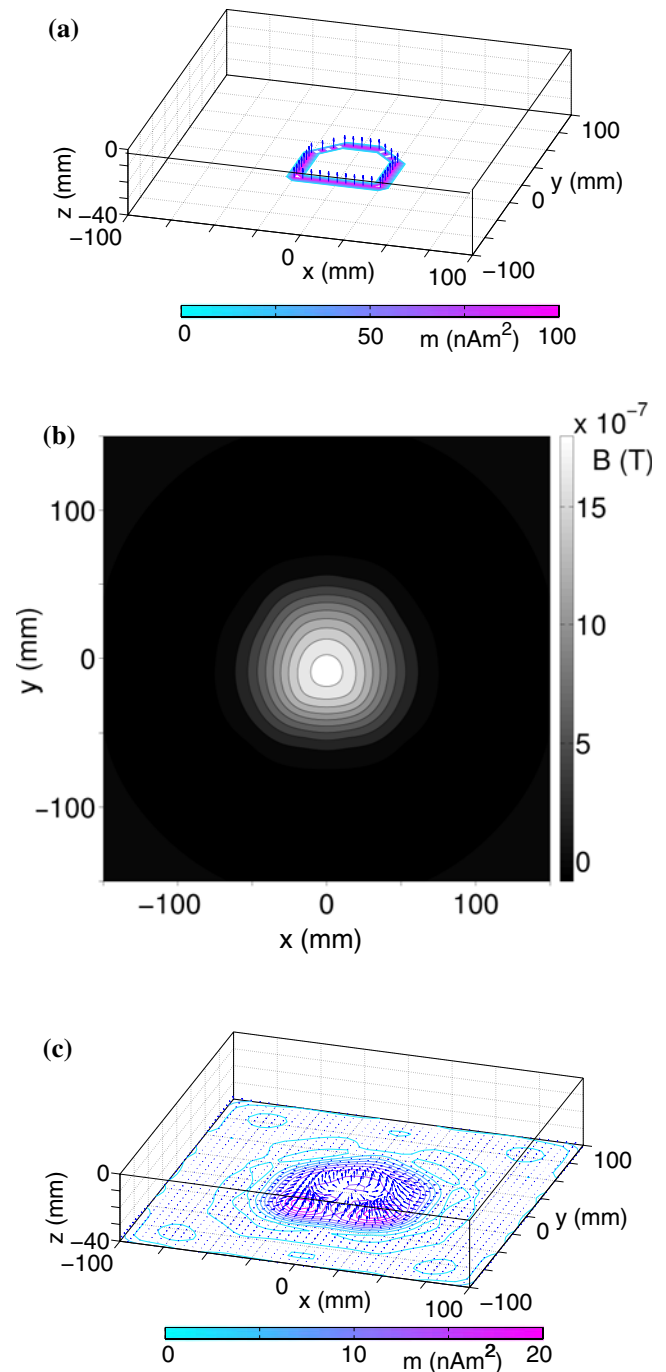


Fig. 1 Example dipole configuration (a), forward computed field (B_z component; PTB sensor configuration) in the lowest sensor plane (b) and reconstruction from noise-free data (c)

a magnetite core and coated with streptavidin were used for the detection of the bound *S. sobrinus*.

Since streptavidin possesses four high affinity binding sites for biotin, biotinylated anti-*S. sobrinus* antibody was coupled to the magnetic nanoparticle and passed over the polyethylene filters. The different concentrations of antigen resulted in the binding of variable amounts of magnetic

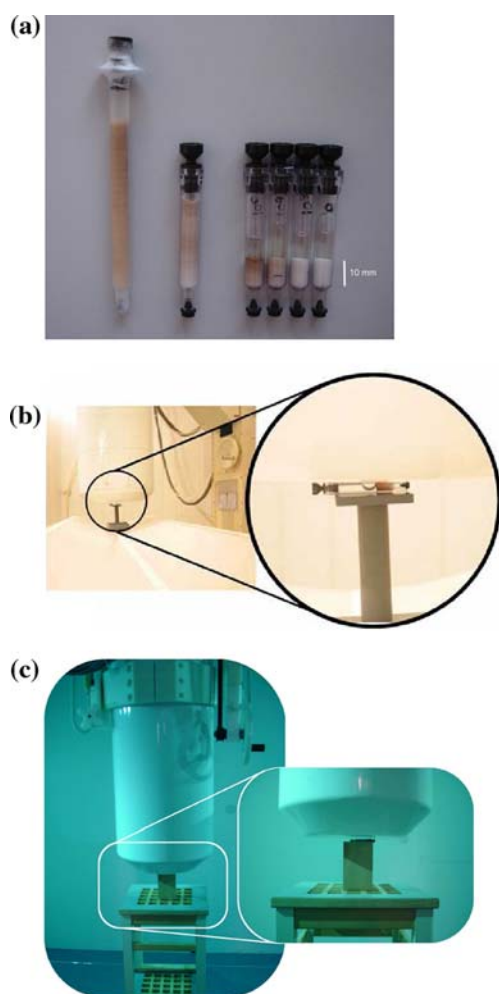


Fig. 2 Nanoparticle column phantoms of lengths 60, 35 and 10 mm (a) and the measurement setup at the Biomagnetic Center Jena (b) and the PTB Berlin (c) with the nanoparticle columns positioned under the dewars containing the SQUIDS

nanoparticles which could subsequently be detected. The columns produced were 10–60 mm in length. A gradient of the nanoparticles was observed in the longer columns, which possibly results from the stacking of smaller filters over one another and a consequent reduction of flow or from non-specific binding of the nanoparticles to the filters.

2.4 Phantom measurement setups

For the phantom measurements we employed SQUID systems as the most sensitive technique available today together with magnetic shielding. The measurements were performed at two different sites. In the Biomagnetic Center at the Friedrich Schiller University Jena a 195 channel Vector-Biomagnetometer ATB Argos 200 [7] was used (Fig. 2b). The SQUIDS are arranged in orthogonal triplets in four planes. The lowest level contains 56 triplets with a mean distance of 27 mm and a measurement plane

diameter of 230 mm. Located parallel above this level in distances of 98, 196 and 254 mm, respectively, are one plane containing seven and two planes each containing one sensor triplets. The measurement system is positioned within a magnetically shielded room, consisting of three highly permeable shieldings and one eddy current shielding.

A 304 channel Vector-Magnetometer [23] in the strongly magnetically shielded room BMSR-2 [25] with seven magnetic layers of mu-metal, one highly conductive Aluminum eddy current layer and active shielding was used at the Physikalisch-Technische Bundesanstalt (PTB) Berlin (Fig. 2c). Here, the SQUIDS are grouped in 19 modules with a total sensor area diameter of 250 mm. In each module the sensors are arranged in four levels. The distance between the closest sensors measuring the same field component is 29 mm. Both setups allow for the measurement of all three spatial components of the magnetic field.

The measurements procedure was the same at both sites: The columns were magnetized in a static field generated by a Neodym permanent magnet (Jena; surface flux density: 380 mT) or a Helmholtz coil (Berlin; field intensity: 1 mT). To minimize the influence of the magnetic relaxation and to ensure remanence measurements, the columns were positioned under the sensor system a few minutes after removing the magnet or switching off the magnetic field. The distance between the bottom sensor layer and the columns was between 30 and 40 mm. The remanence field of each of the columns was measured in different positions and orientations. A baseline was measured before and after every column and used for the correction of the measured data. For each column orientation the signal was averaged over 10 s in order to suppress noise influences (sampling rate: 1 kHz).

3 Results

3.1 Reconstruction from simulated data

The source configuration we simulated and a reconstruction from the forward computed data is shown in Fig. 1. The D-shape formed by the dipoles can still be recognized in the reconstruction although it appears evidently blurred. The total amplitudes are 3,500 nAm² for the simulation and 3,374 nAm² for the reconstruction. Figure 3 shows forward computed data (PTB sensor configuration) for the same source but superimposed with white Gaussian noise (a). The signal-to-noise ratio (SNR) of the simulation is 40 dB. Also displayed in Fig. 3 is the reconstruction from this noisy data (center). The shape of the source can still be recognized but appears noticeably more disturbed. The

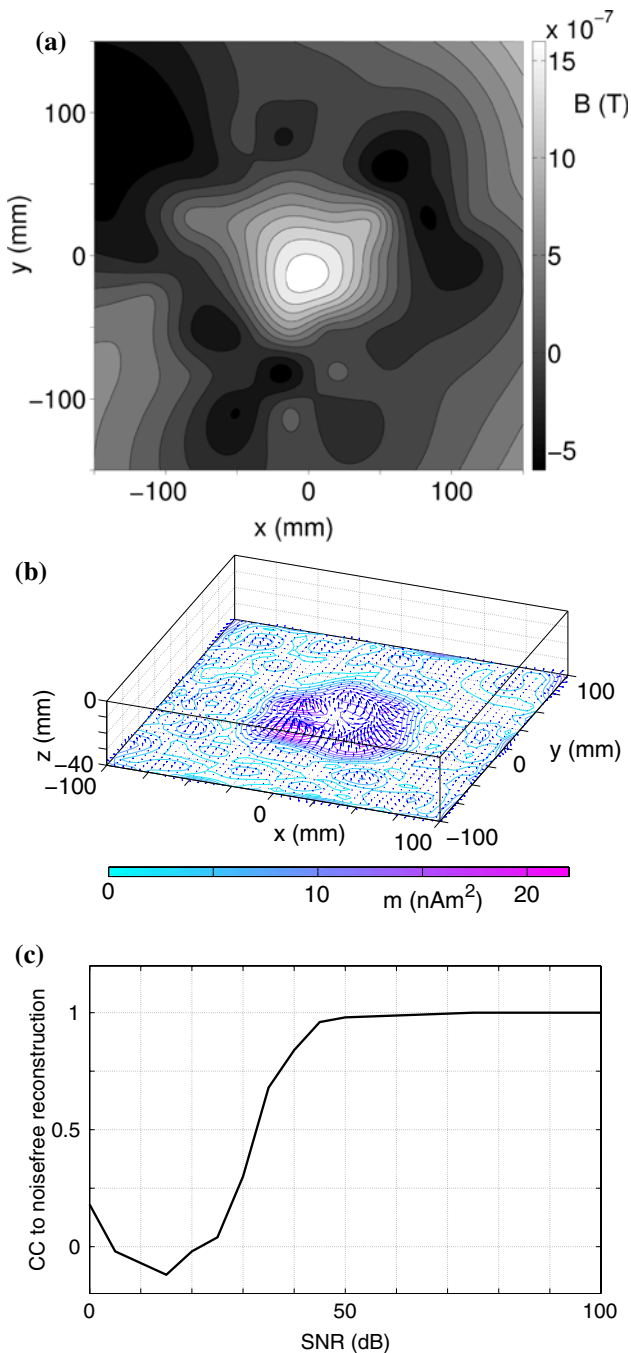


Fig. 3 Influence of noise on the reconstruction quality: Simulated field (B_z component; PTB sensor configuration) with a signal-to-noise ratio of 40 dB (a); reconstruction from noisy simulation (b); correlation coefficients between reconstructions from noise-free data and data with different SNRs (c)

general influence of noise on the reconstruction quality is evaluated by the correlation between a reconstruction from noise-free data and reconstructions from data with different SNRs. Figure 3b shows the computed correlation for SNRs between 0 and 100 dB. It can be seen that for the given sensor setup and source configuration a SNR of at least

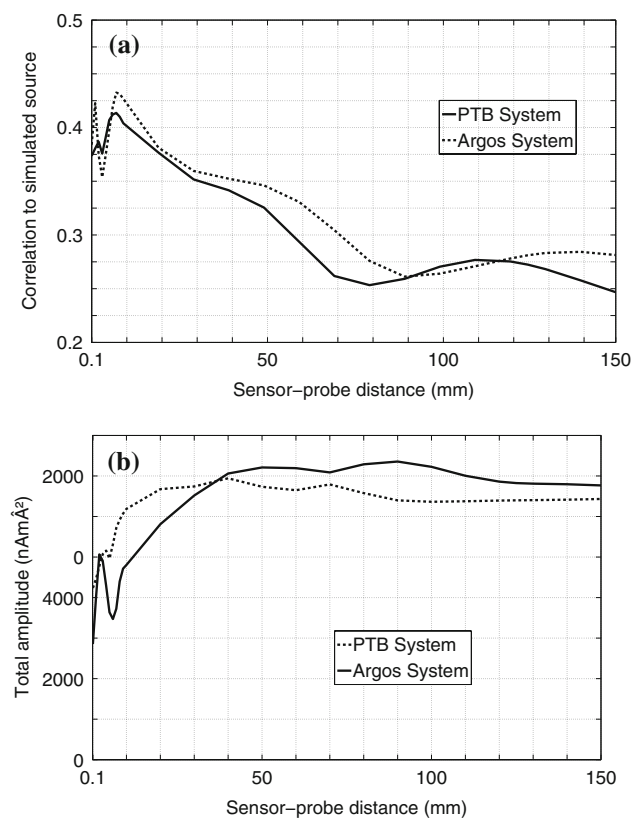


Fig. 4 Influence of the sensor-source distance: correlation coefficients between simulated and reconstructed sources (a) and total amplitude of the reconstruction (b) for sensor-source distances of 1–150 mm

35 dB is required to gain a correlation larger than 50%. For SNRs higher than 50 dB the correlation coefficient approaches 1.

Furthermore, the influence of the distance between source and sensors was investigated. The correlation coefficients between the source, that was noise-free simulated using both sensor configurations, and the respective reconstruction for sensor-source distances of 1–150 mm are displayed in Fig. 4a. The absolute values of the single correlation coefficients are in the range of 0.25–0.5. These low values reflect the principle blurring introduced by the MNEs. With respect to the sensor-source distance, primarily the relation between the coefficients has to be considered.

Regarding the given structure and size of the source and the involved sensor setups, the highest correlation coefficient and thereby the best reconstruction quality can be achieved with the source in a plane approximately 7 mm below the bottom sensor layer. With larger distances, the correlation coefficients decrease significantly except for a minor peak at 110 or 140 mm, respectively. This peak is caused by the upper sensor layers in both systems.

The total amplitudes of these reconstructions are illustrated in Fig. 4b. Only for distances larger than 30 mm the total amplitude of the simulated source ($3,500 \text{ nAm}^2$) can be approximated using both sensor configurations with the applied grid spacing.

For the choice of an appropriate grid related to the size of our phantoms that allows for a reconstruction without loss of information, computations with different grid spacings were compared. Figure 5a shows the correlation coefficients of reconstructions with different grid spacings to one with a grid spacing of 1 mm. Evidently, the correlation coefficient decreases with larger distances between the grid nodes. The loss of information using a grid spacing of 5 mm can be estimated to 0.5%. The total amplitudes of the reconstructions in Fig. 5b do not show a dependence from the choice of the grid spacing. The deviance from the total amplitude of the simulated source ($3,500 \text{ nAm}^2$) is caused by the sensor-source distance of 40 mm, as described above.

3.2 Reconstruction from phantom measurements

The positions and orientations for the measurements of a 35 mm nanoparticle column (antigen concentration 10^5 ml^{-1})

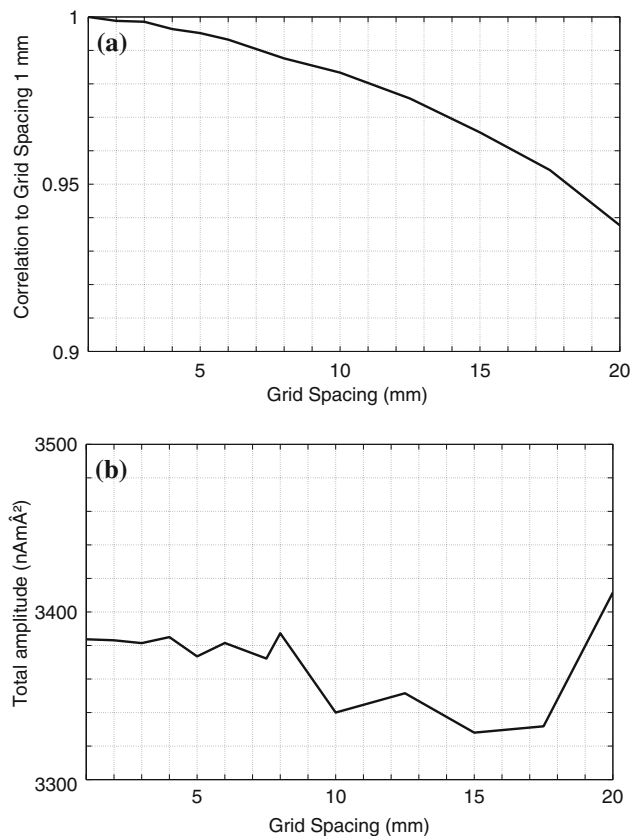


Fig. 5 Influence of the grid spacing on the reconstruction quality: correlation coefficients to a reconstruction using a grid spacing of 1 mm (a) and total amplitude (b) for reconstructions using grid spacings from 2 to 20 mm

with the PTB system are listed in Table 1. Figure 6a and c shows examples for the measurement of this column at both measurement sites. Displayed are the interpolated fields in the bottom sensor layer for the column positioned with its remanence field in vertical direction. The signal of the column can easily be detected in both examples as it could in all data sets. The parameters of the dipoles localized from the PTB measurements are also displayed in Table 1. The dipole positions agree with the real positioning of the column, the orientations are consistent with the column's magnetization orientation. The explained variance is above 95% for all column positions and orientations. Based on the dipole properties we set the reconstruction plane to $z = -40 \text{ mm}$ for all reconstructions. From the Argos data no valid dipole localization was possible due to a lower SNR. The reconstruction plane was thus estimated to $z = -40 \text{ mm}$. A grid spacing of 5 mm was defined for reconstructions from both measurement systems.

The results of the minimum norm reconstructions for the displayed examples are shown in Fig. 6b and d. Again the dipole vectors in the grid nodes are displayed together with their amplitude. It can be clearly seen that the dipoles near the real position of the column show the largest amplitudes and point in the direction of its magnetic field. From these dipoles' amplitudes the longitudinal extent of the columns, their orientation and the predominant magnetic moments can be recognized in both figures. However, the rectangular projection of their tubular shape onto the reconstruction plane can not be recovered.

The parameters of the reconstructed distributions are presented in Table 1. The distances between the localized dipole positions and the computed centroids amount between 2.31 and 11.41 mm and are smaller for the columns with vertical magnetic field. Comparing the magnitude of the localized dipole to the total amplitude of the distribution it can be stated that these values agree well in most cases (deviation 2–16%). The deviations are smaller for the columns with horizontal field (2%) compared to the columns with horizontal field (3–16%).

The results of the localization and reconstructions of the other columns are similar to the findings above. The location of the 10 mm columns can be determined, while the reconstructions produce just ellipsoidal shapes due to their small extent. Decreasing the antigen concentration in the columns, the remanence signal and therewith the reconstruction quality attenuated due to a reduced SNR.

4 Discussion

Minimum norm estimates as a special case of the linear estimation approach are a common method for the reconstruction of distributed current sources from the magnetic

Table 1 Parameters of localized dipoles and reconstructed distributions; distance between localized dipole position and centroid of the reconstruction for 35 mm column measured with PTB system

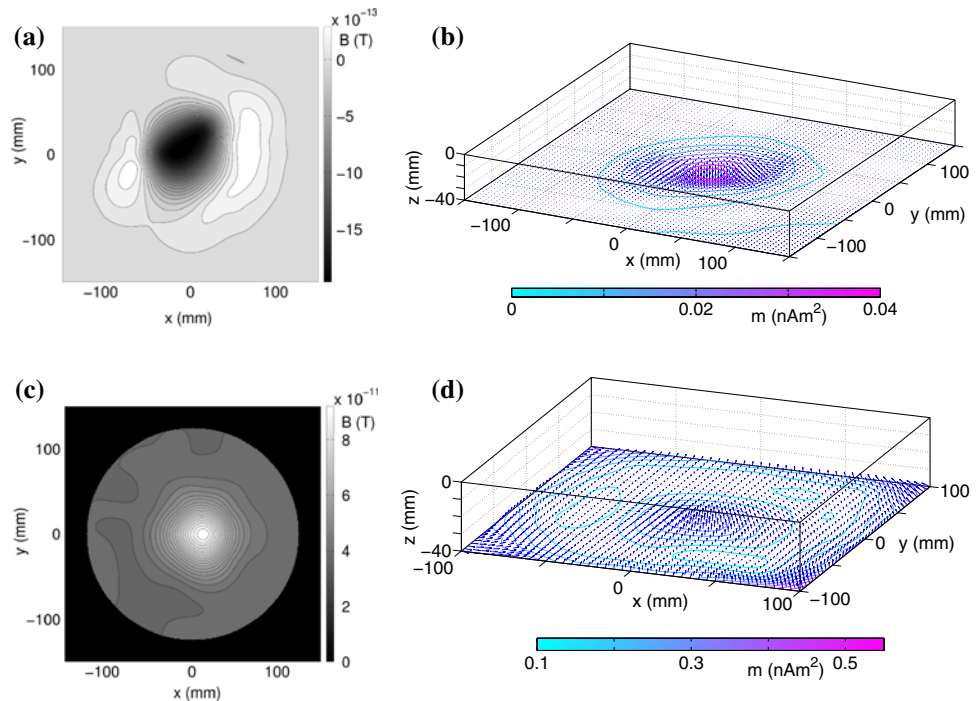
Column orientation	Dipole parameters	Reconstruction parameters	3D distance between dipole and centroid (mm)
Direction 1: horizontal magnetic field	$px_d = 8.61$ mm $py_d = -3.15$ mm $pz_d = -38.02$ mm $ox_d = 0.35$ $oy_d = -0.94$ $oz_d = 0.04$ $m_d = 26.20$ nAm ² $v = 95.19\%$	$px_c = 6.86$ mm $py_c = 7.95$ mm $pz_c = -40.00$ mm $a = 26.63$ nAm ²	$d = 11.41$
Direction 1: vertical magnetic field	$px_d = 2.61$ mm $py_d = -3.08$ mm $pz_d = -37.97$ mm $ox_d = 0.17$ $oy_d = -0.25$ $oz_d = -0.95$ $m_d = 27.03$ nAm ² $v = 97.40\%$	$px_c = 4.26$ mm $py_c = -3.69$ mm $pz_c = -40.00$ mm $a = 22.83$ nAm ²	$d = 2.66$
Direction 2: horizontal magnetic field	$px_d = 1.24$ mm $py_d = 5.86$ mm $pz_d = -38.37$ mm $ox_d = 0.98$ $oy_d = 0.14$ $oz_d = -0.17$ $m_d = 25.58$ nAm ² $v = 97.16\%$	$px_c = -6.59$ mm $py_c = 4.66$ mm $pz_c = -40.00$ mm $a = 25.09$ nAm ²	$d = 8.08$
Direction 2: vertical magnetic field	$px_d = -1.87$ mm $py_d = 8.09$ mm $pz_d = -37.91$ mm $ox_d = -0.03$ $oy_d = 0.34$ $oz_d = 0.94$ $m_d = 22.20$ nAm ² $v = 96.23\%$	$px_c = -1.92$ mm $py_c = 9.24$ mm $pz_c = -40.00$ mm $a = 21.52$ nAm ²	$d = 2.31$

$px_d - pz_d$: dipole position;
 $ox_d - oz_d$: dipole orientation;
 m_d : magnitude; v : explained variance; $px_c - py_c$: position of the centroid of the distribution; a : amplitude of the reconstruction

field without a priori knowledge [11, 18, 28]. In this paper, we applied a similar minimum norm algorithm to simulations and measurements of the remanence field that is generated by magnetic nanoparticles. Our aim was to examine the performance of this technique for Magnetic Nanoparticle Imaging and evaluate the influence of noise, grid spacing and sensor-source distances on the reconstruction quality. The results show that the minimum norm approach is suitable for the reconstruction of magnetic nanoparticle distributions. For high SNRs and small sensor-source distances, it is able to reconstruct the original source shapes, though it is generally restricted by blurring effects due to the applied static dipole model and the algorithm itself.

As could be demonstrated by computer simulations with noise-free data, a perfect (lossless) reconstruction is not possible due to blurring effects. These are even increased in the presence of noise. From examinations with different noise levels it can be estimated that a SNR of at least 35 dB is required to gain an adequate correlation to a noiseless reconstruction. We speculate that an incorporation of noise statistics into the reconstruction scheme as it is provided by linear estimation theory [24] will further enhance the reconstruction results. The inverse computations from simulations with different sensor-source distances prove that this distance has a large effect on the results. A distance of 7 mm between the source and the bottom sensor layer allows for the best reconstruction. With larger sensor-source

Fig. 6 Measured field (B_z component) interpolated in the bottom sensor layer (**a, c**) and computed reconstruction of the distributed sources (**b, d**) of 35 mm column phantom at PTB (*top*) and BioMag (*bottom*)



distances, the reconstruction quality decreases except for a minor peak caused by the upper layers of the used sensor configurations. This distance dependence reflects the recognizability of the simulated source structure in the reconstructions, which depends not only on the correlation coefficient but also on the shape of the source itself. In contrast to the correlation, the total amplitude of the reconstruction is lower for small sensor-probe distances. A distance of at least 30 mm would be required to reconstruct the amplitude of the source with a deviation of less than 10%.

Also investigated was the influence of the grid spacing on the reconstruction quality. Increasing distances between the nodes of the reconstruction grid cause a decrease of the reconstruction quality. A grid spacing of 5 mm can be considered adequate. Higher resolutions would not improve the reconstructions quality in terms of the correlation to a 1 mm grid reconstruction and the graphical representation of the distributions. However, they would increase the computational effort noticeably. In contrast, the choice of the grid spacing does not affect the total amplitude of the reconstructed sources. Another important issue is the dimension of the grid. As can be seen from Fig. 6d, large edge effects occur if the grid's extension is too small. The same was described by Brauer et al. [4] who observed very large currents at the borders of minimum norm reconstructions of extended primary current sources if their dimension was less than five times the source dimension. All findings above are valid for the given sensor setups and the simulated sources. Their shape and dimension can be considered representative for real in vivo distributions. Therefore, and since the involved sensor

setups are common for today's measurement system, all findings can be transferred to similar measurement setups and to in vivo measurements.

The results of the phantom measurement reconstruction prove that nanoparticle distributions with the given dimensions can be computed from measured magnetic remanence fields. The properties of the dipoles that were localized from the measurements comply very well with the positioning of the phantoms for the PTB system. For the measurements with the Argos system, a useful dipole localization is not possible which is primarily caused by a lower SNR due to higher environmental noise levels. The shape of the sources can be recognized in the distributions reconstructed from data of both measurement systems, though the algorithm is not able to reconstruct the rectangular shape of the phantoms' projection on the reconstruction plane. The small distances between the localized dipole positions and the centroids of the distributions, especially for the columns with vertical field, show that the minimum norm approach can detect the location of the distributions with a deviation of less than 10 mm. Our results show a consistency between the localized dipole magnitude and the total amplitude of the distributions. This suggests that a quantification of the distributions might be possible, though this has to be investigated in further studies.

5 Conclusions

Our results show that the approach of using MNEs is suitable for magnetic nanoparticle imaging. Our parameter

studies quantifying the influence of noise, sensor-source distance and grid-spacing set the basis for future in vitro and in vivo studies. Improvements in the reconstruction quality are expected from the development of sophisticated regularization schemes and appropriate post-processing algorithms.

Acknowledgments This work was funded by the E. C. Sixth Framework Programme (STREP project “Biodiagnostics”, contract no. NMP4-CT-2005-017002) and in part supported by the the German Federal Ministry of Education and Research (FKZ 13N9150) and the state of Thuringia under participation of the European Funds for Regional Development (TAB project 2006FE0096).

References

1. A generic environment for bio-numerical simulation. ist-program of the european commission, project no. 10378 (2000) <http://www.simbio.de>
2. Alexiou C, Schmid R, Jurgons R, Bergemann C, Arnold W, Parak F (2002) Ferrofluids—magnetically controllable fluids and their applications, Lecture Notes in Physics, vol 594. Targeted tumor therapy with “Magnetic Drug Targeting”: therapeutic efficacy of ferrofluid bound mitoxantrone. Springer, Berlin, pp 233–251
3. Apel M, Heinlein UA, Miltenyi S, Schmitz J, Campbell JD (2007) Magnetism in medicine, 2 edn. Magnetic cell separation for research and clinical applications. Wiley-VCH, Berlin, pp 571–595. doi:10.1002/9783527610174.ch4g
4. Brauer H, Haueisen J, Ziolkowski M, Tenner U, Nowak H (2000) Reconstruction of extended current sources in a human body phantom applying biomagnetic measuring techniques. IEEE Trans Magn 36(4):1700–1705. doi:10.1109/20.877770
5. Bulte JWM, Kraitchman DL (2004) Iron oxide mr contrast agents for molecular and cellular imaging. NMR Biomed 17(7):484–499. doi:10.1002/nbm.924
6. Dames P, Gleich B, Flemmer A, Hajek K, Seidl N, Wiekhorst F, Eberbeck D, Bittmann I, Bergemann C, Weyh T, Trahms L, Rosenacker J, Rudolph C (2007) Targeted delivery of magnetic aerosol droplets to the lung. Nat Nano 2(8):495–499. doi:10.1038/nnano.2007.217
7. Di Rienzo L, Haueisen J (2006) Theoretical lower error bound for comparative evaluation of sensor arrays in magnetostatic linear inverse problems. IEEE Trans Magn 42(11):3669–3673. doi:10.1109/TMAG.2006.882338
8. Enpuku K, Soejima K, Nishimoto T, Tokumitsu H, Kuma H, Hamasaki N, Yoshinaga K (2006) Liquid phase immunoassay utilizing magnetic marker and high t-c superconducting quantum interference device. J Appl Phys 100(5). doi:10.1063/1.2337384
9. Flynn ER, Bryant HC (2005) A biomagnetic system for in vivo cancer imaging. Phys Med Biol 50:1273–1293. doi:10.1088/0031-9155/50/6/016
10. Gleich B, Weizenecker J (2005) Tomographic imaging using the nonlinear response of magnetic particles. Nature 435(7046):1214–1217. doi:10.1038/nature03808
11. Hämläinen MS, Ilmoniemi RJ (1994) Interpreting magnetic-fields of the brain—minimum norm estimates. Med Biol Eng Comput 32(1):35–42. doi:10.1007/BF02512476
12. Hansen PC (1987) The truncated svd as a method for regularization. BIT 27(4):534–553. doi:10.1007/BF01937276
13. Haueisen J, Unger R, Beucker T, Bellemann M (2002) Evaluation of inverse algorithms in the analysis of magnetic flux leakage data. IEEE Trans Magn 38(3):1481–1488. doi:10.1109/20.999121
14. Hergt R, Dutz S, Miller R, Zeisberger M (2006) Magnetic particle hyperthermia: nanoparticle magnetism and materials development for cancer therapy. J Phys Condens Matter 18(38):2919–2934. doi:10.1088/0953-8984/18/38/S26
15. Ito A, Shinkai M, Honda H, Kobayashi T (2005) Medical application of functionalized magnetic nanoparticles. J Biosci Bioeng 100(1):1–11
16. Johannsen M, Gneveckow U, Thiesen B, Taymoorian K, Cho C, Waldoefner N, Scholz R, Jordan A, Loening S, Wust P (2007) Thermotherapy of prostate cancer using magnetic nanoparticles: feasibility, imaging, and three-dimensional temperature distribution. Eur Urol 52(6):1653–1662. doi:10.1016/j.eururo.2006.11.023
17. Jordan A, Scholz R, Wust P, Fahling H, Krause J, Wlodarczyk W, Sander B, Vogl T, Felix R (1997) Effects of magnetic fluid hyperthermia (mfh) on c3h mammary carcinoma in vivo. Int J Hyperther 13(6):587–605
18. Leder U, Haueisen J, Huck M, Nowak H (1998) Non-invasive imaging of arrhythmogenic left-ventricular myocardium after infarction. Lancet 352(9143):1825–1825. doi:10.1016/S0140-6736(98)00082-8
19. Pankhurst Q, Connolly J, Jones S, Dobson J (2003) Applications of magnetic nanoparticles in biomedicine. J Phys Appl Phys 36(13):R167–R181(1). doi:10.1088/0022-3727/36/13/201
20. Pinto B, Silva C (2007) A simple method for calculating the depth of eeg sources using minimum norm estimates (mne). Med Biol Eng Comput 45(7):643–652. doi:10.1007/s11517-007-0204-z
21. Rad A, Arbab A, Iskander A, Jiang Q, Soltanian-Zadeh H (2007) Quantification of superparamagnetic iron oxide (spio)-labeled cells using mri. J Magn Reson Imag 26(2):366–374. doi:10.1002/jmri.20978
22. Salata OV (2004) Applications of nanoparticles in biology and medicine. J Nanobiotechnol 2:3. doi:10.1186/1477-3155-2-3
23. Schnabel A, Burghoff M, Hartwig S, Petsche F, Steinhoff U, Drung D, Koch H (2004) A sensor configuration for a 304 squid vector magnetometer. Neurol Clin Neurophysiol 70
24. Smith WE, Dallas WJ, Kullmann WH, Schlitt HA (1990) Linear estimation theory applied to the reconstruction of a 3-d vector current distribution. Appl Opt 29(5):658–667
25. Thiel F, Schnabel A, Knappe-Grüneberg S, Stollfu D, Burghoff M (2007) Demagnetization of magnetically shielded rooms. Rev Sci Instrum 78(3):035,106. doi:10.1063/1.2713433
26. Thorek D, Chen A, Czupryna J, Tsourkas A (2006) Superparamagnetic iron oxide nanoparticle probes for molecular imaging. Ann Biomed Eng 34(1):23–38. doi:10.1007/s10439-005-9002-7
27. Tikhonov AN (1963) Resolution of ill-posed problems and the regularization method (in russian). Dokl Akad Nauk SSSR 151:501–504
28. Uchida S, Iramina K, Goto K, Ueno S (2000) A comparison of iterative minimum norm estimation and current dipole estimation for magnetic field measurements from small animals. IEEE Trans Magn 36(5):3724–3726. doi:10.1109/20.908953
29. Varah JM (1973) On the numerical solution of ill-conditioned linear systems with applications to ill-posed problems. SIAM J Numer Anal 10(2):257–267. doi:10.1137/0710025
30. Weitschies W, Ktitz R, Bunte T, Trahms L (1997) Determination of relaxing or remanent nanoparticle magnetization provides a novel binding specific technique for the evaluation of immunoassays. Pharm Pharmacol Lett 7:5–8
31. Wiekhorst F, Jurgons R, Eberbeck D, Seliger C, Steinhoff U, Trahms L, Alexiou C (2006) Quantification of magnetic nanoparticles by magnetorelaxometry after local cancer therapy with magnetic drug targeting. J Nanosci Nanotechnol 6(9–10):3222–3225. doi:10.1166/jnn.2006.477